Zhongyi Deng[1]
Rui Xiao[1]
Baosheng Jin[1]
Qilei Song[1]
He Huang[2]

[1] Key Laboratory of Clean Coal Power Generation and Combustion Technology of the Ministry of Education, Southeast University, Nanjing, P. R. China.

[2] College of Life Science and Pharmacy, Nanjing University of Technology, Nanjing, P. R. China.

Research Article

Multiphase CFD Modeling for a Chemical Looping Combustion Process (Fuel Reactor)

There are growing concerns about increasing emissions of greenhouse gases and a looming global warming crisis. CO_2 is a greenhouse gas that affects the climate of the earth. Fossil fuel consumption is the major source of anthropogenic CO_2 emissions. Chemical looping combustion (CLC) has been suggested as an energy-efficient method for the capture of carbon dioxide from combustion. A chemical-looping combustion system consists of a fuel reactor and an air reactor. The air reactor consists of a conventional circulating fluidized bed and the fuel reactor is a bubbling fluidized bed. The basic principle involves avoiding direct contact of air and fuel during the combustion. The oxygen is transferred by the oxygen carrier from the air to the fuel. The water in combustion products can be easily removed by condensation and pure carbon dioxide is obtained without any loss of energy for separation. With the improvement of numerical methods and more advanced hardware technology, the time required to run CFD (computational fluid dynamic) codes is decreasing. Hence, multiphase CFD-based models for dealing with complex gas-solid hydrodynamics and chemical reactions are becoming more accessible. To date, there are no reports in the literature concerning mathematical modeling of chemical-looping combustion using FLUENT. In this work, the reaction kinetics models of the ($CaSO_4$ + H_2) fuel reactor is developed by means of the commercial code FLUENT. The effects of particle diameter, gas flow rate and bed temperature on chemical looping combustion performance are also studied. The results show that the high bed temperature, low gas flow rate and small particle size could enhance the CLC performance.

Keywords: Chemical looping combustion, CFD modeling, CO_2 capture, $CaSO_4$

Received: July 15, 2008; *revised:* August 14, 2008; *accepted:* August 15, 2008

DOI: 10.1002/ceat.200800341

1 Introduction

The possible linkage between rising levels of atmospheric carbon dioxide and global warming has led to international agreements to reduce carbon dioxide emissions. The main contributor to the increases in atmospheric CO_2 concentration is fossil fuel combustion for power generation, transport, industry, and domestic use. About a third of the global CO_2 emissions come from combustion of fossil fuels in power generation.

One option for reducing emissions of CO_2 to the atmosphere and still enabling using fossil fuel use as an energy source is to separate and dispose of the CO_2 from combustion. Disposal costs are generally low, but the separation of CO_2 involves significant costs. The concentration of CO_2 in the flue gas of a conventional combustion system is only 10–14 %. There are a number of techniques that can be used to separate CO_2 from the flue gas. The main disadvantage of these techniques is the large amount of energy required for CO_2 separation. For a coal-fired power plant, ca. 15–20 % of the electricity produced will be lost to CO_2 separation due to its low concentration in the flue gas. Chemical-looping combustion (CLC) has been proposed as a new technology that would satisfy the urgent need [1]. It is indirect combustion whereby oxygen (from air) is transferred by a solid oxygen carrier to fuel combustion. In a CLC process, fuel gas is burnt in two reactors designated as the fuel and air reactors. An oxide, which circulates between the air reactor and fuel reactor, acts as the oxygen carrier. The oxygen is transferred by the oxygen carrier from the air to the fuel. The water in combustion products can be easily removed by condensation and pure carbon dioxide is obtained without any loss of energy due to separation. Many research works have been carried out on this field [2], e.g., oxygen car-

Correspondence: Dr. Z. Y. Deng (dzyseu@gmail.com), Key Laboratory of Clean Coal Power Generation and Combustion Technology of the Ministry of Education, Southeast University, Nanjing 210096, P. R. China.

rier development, system analysis and reactor design. The CLC process should be a good candidate for the production of clean energy from fossil fuel.

Recent studies in this novel technology [3–10] have been focused in three distinct areas, i.e., techno-economic evaluations, integration of the system into power plant concepts, and experimental development of oxygen carrier metals, e.g., Fe, Ni, Mn, Cu, and Ca. The oxygen carrier is a core technology in the CLC system. The current oxygen carriers are metal oxides that have high reactivity and stability. However, these metal-oxide oxygen carriers will inevitably have some leakage to the environment and become secondary pollution sources.

$CaSO_4$ has many advantages as a novel oxygen carrier. It is much more environmentally friendly as a nonmetal oxide. $CaSO_4$ is cheaper due to vast gypsum resources all over the world. Compared with metal oxides, $CaSO_4$ has a relatively higher oxygen capacity. The oxygen ratio R_O, which is defined as $R_O = (m_{ox} - m_{red})/m_{ox}$, represents the oxygen transport capacity. The value of R_O for pure $CaSO_4$ is 0.4706, which is much higher than that of many other metal oxides [11]. In addition, natural anhydrite ore, one type of gypsum resource, has a higher mechanical strength and is very suitable for use in fluidized-bed reactors of the chemical-looping combustion system.

The concept of directly using of $CaSO_4$ as a novel oxygen carrier in chemical-looping combustion is shown in Fig. 1. A chemical-looping combustion design using two interconnected fluidized-bed reactors is shown in Fig. 2.

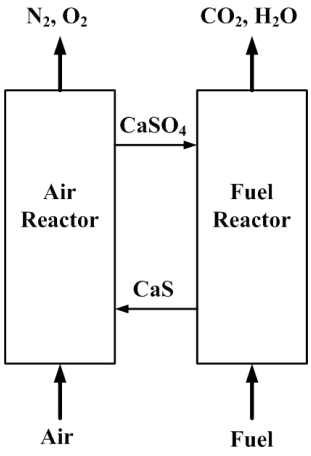

Figure 1. Concept view of chemical-looping combustion using $CaSO_4$ as oxygen carrier.

Calcium sulfate ($CaSO_4$) is reduced by hydrogen (H_2), methane (CH_4) and carbon monoxide (CO) to calcium sulphide (CaS) in the fuel reactor, as given in Eqs. (1–3):[1)]

$$CaSO_4 + 4H_2 \rightarrow CaS + 4H_2O \quad (1)$$

$$CaSO_4 + 4CO \rightarrow CaS + 4CO_2 \quad (2)$$

$$CaSO_4 + 4CH_4 \rightarrow CaS + CO_2 + 2H_2O \quad (3)$$

1) List of symbols at the end of the paper.

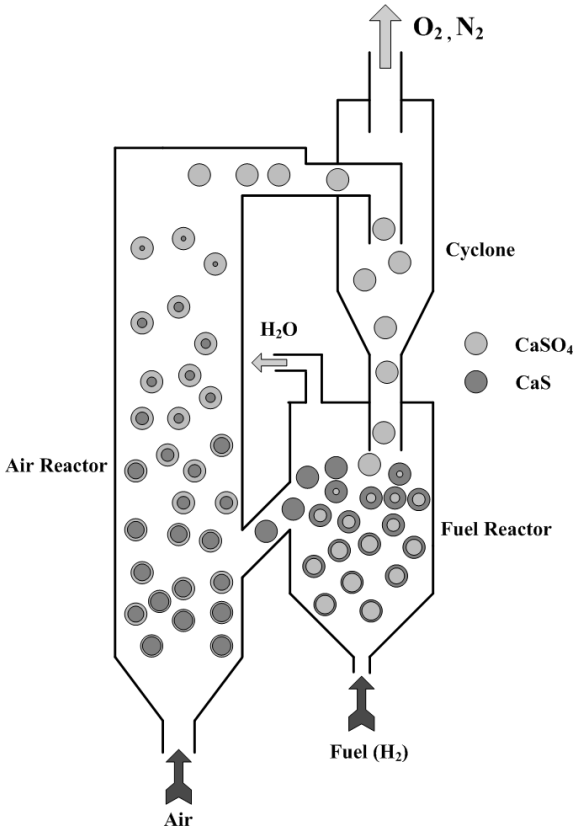

Figure 2. Chemical-looping combustion with two interconnected fluidized-bed reactors.

The reduction reaction produces only carbon dioxide and water vapor, and CO_2 can be easily separated and collected by cooling the exhaust gas. In addition to reactions (1–3), the parallel reactions (4) and (5) also take place under certain conditions [12]:

$$CaSO_4 + H_2 \rightarrow CaO + H_2O + SO_2 \quad (4)$$

$$CaSO_4 + CO \rightarrow CaO + CO_2 + SO_2 \quad (5)$$

With the improvement of numerical methods and more advanced hardware technology, the time required to run CFD codes is decreasing. Hence, multi-dimensional models for dealing with complex gas-solid hydrodynamics, heat transfer and chemical reactions are becoming more accessible. Once the model has been validated, CFD can be used to undertake sensitivity analysis as it provides the flexibility to change parameters. A series of unsteady, three-fluid CFD models were performed using FLUENT 6.0 by Cooper and Coronella [13] to simulate particle mixing in a binary fluidized-bed. Ravelli et al. [14] have proposed a mathematical model to simulate the combustion of refuse-derived fuel (RDF) in a bubbling fluidized bed by means of the commercial code FLUENT 6.1 and the predicted and the experimental data are seen to be in good agreement. Frazeli and Behnam [15] have proposed a CFD model to predict methane autothermal in a catalytic microreactor.

A recent thorough literature review by the current authors showed that multiphase fluid dynamics modeling for CLC by FLUENT is not available in the open literature. In this study, the reaction kinetic models of the ($CaSO_4$ + H_2) fuel reactor have been developed to mimic the behavior of reactive flow in the reactors. The effect of bed temperature on chemical looping combustion performance is also studied. The results show that the higher bed temperature could enhance the CLC performance.

The focus of this paper detailing the performance of the ($CaSO_4$ + H_2) fuel reactor is only a first step in the direct numerical simulation of the entire CLC system. This study does not focus on the combustion of the whole system. Future work will involve coupling the fuel reactor with other components, e.g., the air reactor and cyclone, to model the complete loop system.

2 Mathematical Model

The main assumptions of the model proposed in this work are:

I. It includes two phases, i.e., gas and solid;
II. The particles in the bed are spherical and uniform in size;
III. The particles are assumed to be inelastic and smooth;
IV. The kinetic theory of granular flow (KTGF) is used in transport equation to describe the particle collisions and fluctuations in the bed, and
V. Shen and Zheng [12] suggested that the optimal temperature of the fuel reactor should be below 950 °C in the process of chemical looping combustion, because the parallel reactions (4) and (5) are restricted and very little SO_2 is produced under this condition. In this work, the temperature for most of the cases described below is 950 °C. Therefore, the parallel reactions (4) and (5) are ignored.

2.1 Gas-Solid Hydrodynamics

2.1.1 Continuity Equations

The gas continuity equations for the gas phase and solid phase are given by Eqs. (6) and (7), respectively:

$$\frac{\partial}{\partial t}\left(\varepsilon_g\rho_g\right) + \nabla\left(\varepsilon_g\rho_g V_g\right) = S_{gs} \tag{6}$$

$$\frac{\partial}{\partial t}\left(\varepsilon_s\rho_s\right) + \nabla\left(\varepsilon_s\rho_s V_s\right) = S_{sg} \tag{7}$$

where ε, ρ and V are the volume fraction, the density and the instantaneous velocity, respectively. The instantaneous velocities of particles, V_s, can be substituted by the solid mean velocity, u_s. This form was also derived from the Boltzmann integral-differential equation by Ding and Gidaspow [16]. S is the source term and is only set to zero in the flow field. When the continuity equations are used for heterogeneous reactions, then mass, momentum and heat exchange exist between the gaseous and solid phases.

2.1.2 Momentum Equations

The momentum equation for the gas phase is given by Eq. (8):

$$\frac{\partial}{\partial t}\left(\varepsilon_g\rho_g V_g\right) + \nabla\left(\varepsilon_g\rho_g V_g V_g\right) = -\varepsilon_g\nabla P + \varepsilon_g\rho_g g + \nabla\,\varepsilon_g\tau_g - \beta_{gs}\left(V_g - u_s\right) + S_{gs}u_s \tag{8}$$

where β_{gs} is the drag coefficient between the gas phase and solid phase, g is gravity and u_s is the mean velocity. On the right-hand side of the equation, the fifth term, $S_{gs}u_s$, describes the momentum transfer of the solid. The momentum equation for the solid phase should be useful for obtaining the reverse source term and can be expressed as given in Eq. (9):

$$\frac{\partial}{\partial t}\left(\varepsilon_s\rho_s V_s\right) + \nabla\left(\varepsilon_s\rho_s V_s V_s\right) = -\varepsilon_s\nabla P + \varepsilon_s\rho_s g - \nabla P_s + \nabla\,\varepsilon_s\tau_s + \beta_{gs}\left(V_g - u_s\right) + S_{sg}u_s \tag{9}$$

2.1.3 Energy Equations

The energy equations for the gas phase and solid phase are given by Eqs. (10) and (11), respectively:

$$\frac{\partial}{\partial t}\left(\varepsilon_g\rho_g H_g\right) + \nabla\left(\varepsilon_g\rho_g u_g H_g\right) = \nabla\left(\lambda_g\nabla T_g\right) + Q_{gs} + S_{gs}H_s \tag{10}$$

$$\frac{\partial}{\partial t}\left(\varepsilon_s\rho_s H_s\right) + \nabla\left(\varepsilon_s\rho_s u_s H_s\right) = \nabla\left(\lambda_s\nabla T_s\right) + Q_{sg} + S_{sg}H_s \tag{11}$$

where H, λ and Q are enthalpy, thermal conductivity of the mixture and heat exchange between the gas phase and solid phase, respectively. The third term on the right-hand side of the equation represents the heat transfer involved as the solid phase changes into gas phase.

The heat exchange between phases can be expressed as a function of the temperature difference and agrees with the local balance condition $Q_{sg} = -Q_{gs}$, as follows:

$$Q_{sg} = h_{sg}\left(T_s - T_g\right) \tag{12}$$

where h_{sg} is heat transfer coefficient, which is related to the Nu_s of the solid phase and is given by Eq. (13):

$$h_{sg} = \frac{6k_g\varepsilon_s\varepsilon_g Nu_s}{d_p^2} \tag{13}$$

In Eq.(13), k_g is the thermal conductivity of the gas and Nu_s was proposed by Gunn [17]as given by Eq. (14):

$$Nu_s = (7 - 10\varepsilon_g + 5\varepsilon_g^2)(1 + 0.7Re_s^{0.2}Pr^{1/3}) + 1.33 - 2.4\varepsilon_g + 1.2\varepsilon_g^2)Re_s^{0.7}Pr^{1/3} \tag{14}$$

2.1.4 Kinetic Theory of Granular Flow (KTGF)

A transport equation that describes particle collisions resulting in a random granular motion is defined for the solid phase by Eq. (15) [18]:

$$\frac{\partial}{\partial t}(\varepsilon_s\rho_s\Theta_s) + \nabla\ (\varepsilon_s\rho_s\Theta_s u_s) = -\frac{2}{3}(p_s\bar{\bar{I}} + \varepsilon_s\bar{\bar{\tau}}_s) : \nabla\vec{u}_s + \nabla\ (k_s\nabla\Theta_s) - \gamma - 3\beta_{gs}\Theta_s \quad (15)$$

In Eq. (15), p_s is the solid pressure and Θ_s is the granular temperature, and is defined as:

$$\Theta = \frac{1}{3}\langle u'_s u'_s\rangle \quad (16)$$

where u'_s is the fluctuating velocity of the particles and can be derived from $u'_s = V_s - u_s$. The solid pressure, p_s, is given by:

$$p_s = \varepsilon_s\rho_s\Theta_s + 2(1+e)\varepsilon_s^2 g_0\rho_s\Theta_s \quad (17)$$

where g_0 is the radial distribution function and is given by Eq. (18):

$$g_0 = \frac{3}{5}\left[1 - \left(\frac{\varepsilon_s}{\varepsilon_{s,\max}}\right)^{\frac{1}{3}}\right]^{-1} \quad (18)$$

The dissipation of fluctuating energy due to inelastic collisions takes the form of Eq. (19):

$$\gamma = 3(1-e^2)\varepsilon_s^2\rho_s d_s g_0\Theta_s\left[\frac{4}{d_s}\left(\sqrt{\frac{\Theta_s}{\pi}}\right) - \nabla u_s\right] \quad (19)$$

The remaining term that needs to be considered is the interphase momentum transfer. It is believed that the drag between the gas phase and solid phase plays an important role in the momentum exchange. If $\varepsilon_g < 0.8$, the well-known Ergun equation [17] is suitable for describing the dense regime, Eq. (20):

$$\beta_{gs} = 150\frac{(1-\varepsilon_g)\varepsilon_s\mu_g}{\varepsilon_g d_s^2} + 1.75\frac{\rho_g\varepsilon_s|u_g - u_s|}{d_s} \quad (20)$$

If $\varepsilon_g > 0.8$, the drag coefficient can be evaluated on the basis of the work of Wen and Yu [19] as Eq. (21):

$$\beta_{gs} = \frac{3}{4}C_d\frac{|u_g - u_s|}{d_s}\varepsilon_g^{-2.65} \quad (21)$$

where

$$C_d = \begin{cases}\frac{24}{Re}(1 + 0.15\,Re^{0.687}) & Re \le 1000\\ 0.44 & Re > 1000\end{cases} \quad (22)$$

and

$$R_e = \frac{|u_g - u_s|\varepsilon_g\rho_g d_s}{\mu_g} \quad (23)$$

2.1.5 Species Transport Equations

The transport equations for species in the reactor are summarized by Eq. (24):

$$\frac{\partial}{\partial T}\left(\rho_g\varepsilon_g Y_{g,i}\right) + \nabla\left(\rho_g\varepsilon_g V_g Y_{g,i}\right) = -\nabla\ \varepsilon_g J_{g,i} + R_{s,i} + \varepsilon_g R_{g,i} \quad (24)$$

where $J_{g,i}$, $R_{g,i}$ and $R_{s,i}$ are the diffusion flux of species i in the gas phase, the net rate of production of homogeneous species i and the heterogeneous reaction rate, respectively. In the species transport equations of the gas phase, mass diffusion coefficients are used to calculate the diffusion flux of chemical species in turbulent flow using a modified version of Fick's law, Eq. (25):

$$J_{g,i} = -\left(\rho D_{i,m} + \frac{\mu_t}{Sc_t}\right)\nabla Y_{g,i} \quad (25)$$

where $D_{i,m}$ is the diffusion coefficient of the mixture in m^2/s.

2.2 Constitutive Closure Models

Constitutive relations are needed to close governing relations. The constitutive relations used in the current model are summarized by the equations in the list below.

– Stress tensor of the gas phase:

$$\tau_{g,ij} = \mu_g\left(\frac{\partial V_{g,j}}{\partial x,I} + \frac{\partial V_{g,I}}{\partial x,j}\right) \quad (26)$$

– Stress tensor of the particulate phase:

$$\tau_{s,ij} = \mu_s\left(\frac{\partial V_{s,j}}{\partial x,I} + \frac{\partial V_{s,I}}{\partial x,j}\right) + \left(\xi_s - \frac{2}{3}\mu_p\right)\frac{\partial V_{s,k}}{\partial x,k}\delta_{Ij} - p_s\delta_{Ij} \quad (27)$$

– Diffusion coefficient of granular temperature (Syamlal-O'Brien model):

$$k_{\Theta s} = \frac{15\ d_s\ \rho_s\ \varepsilon_s\ \sqrt{\Theta_s\ \pi}}{4\ (41-33\eta)}\left[1 + \frac{12}{5}\eta^2\ (4\ \eta - 3)\ \varepsilon_s\ g0 + \frac{16}{15\ \pi}(41-33\eta)\ \eta\ \varepsilon_s\ g0\right] \quad (28)$$

$$\eta = \frac{1}{2}(1 + e_{ss}) \quad (29)$$

– Transfer of kinetic energy:

$$\phi_{gs} = -3K_{gs}\Theta_s \quad (30)$$

– Solids pressure:

$$P_s = \varepsilon_s\rho_s\Theta_s + 2\rho_s(1+e_{ss})\ \varepsilon^2{}_s g_0\Theta_s \quad (31)$$

– Solid shear viscosity:

$$\mu_s = \mu_{s,col} + \mu_{s,kin} + \mu_{s,fr} \quad (32)$$

– Solid collision viscosity:

$$\mu_{s,col} = \frac{4}{5}\ \varepsilon_s\ \rho_s\ d_s\ g0\ (1+e_{ss})\ \left(\frac{\Theta_s}{\pi}\right)^{1/2} \quad (33)$$

– Solid frictional viscosity:

$$\mu_{s,fr} = \frac{p_s \sin\phi}{2\sqrt{I_{2D}}} \quad (34)$$

and

– Kinetic viscosity (Syamlal-O'Brien model):

$$\mu_{s,kin} = \frac{d_s \rho_s \varepsilon_s \sqrt{\Theta_s \pi}}{6(3-e_{ss})}\left[1+\frac{2}{5}(1+e_{ss})(3e_{ss}-1)\varepsilon_s g0\right] \quad (35)$$

2.3 Fuel Reactor Kinetic Model

A review of the relevant literature by Kim and Sohn [20] shows that the activation energy for the reduction of calcium sulfate to produce calcium sulfide is 151 kJ/mol. The reaction is of first order with respect to the hydrogen partial pressure for calcium sulfate.

In the current work, the shrinking-core model is applied initially. This model has previously been successfully used to describe the reactivity of the particle [21, 22]. The kinetic equations for the model relating the conversion and time are given by Eqs. (36) and (37):

$$Z_i = \frac{t}{\tau_i} \quad (36)$$

and

$$\frac{dZ_i}{dt} = \frac{1}{\tau_i} \quad (37)$$

where τ_i is the time for complete conversion of the particle for the reaction i and is calculated from Eq. (38):

$$\tau_i = \frac{1}{K_i P_{H_2}} \quad (38)$$

In Eq. (38), K_i is the apparent kinetic constant and is given by Eq. (39) [20]:

$$K_i = 4.3\times10^3 e^{\left(-\frac{151000}{RT}\right)} \quad (39)$$

It has been assumed that the reaction rate is first order with respect to hydrogen and is given as follows, Eq. (40):

$$r_c = \rho_{m,CaSO_4}\frac{dZ_i}{dt} \quad (40)$$

3 Simulation Method

3.1 Simulation Code and Numerical Algorithm

The differential equations mentioned in the previous section were solved by a finite volume method. These equations were discretized by an upwind differencing scheme over the finite volume used, and solved by the commercial CFD software code Fluent 6.2.16. A time step of 0.0001 s was chosen. This iteration was adequate to achieve convergence for the majority of time steps. First-order discretization schemes for the convection terms were used. The relative error between two successive iterations was specified by using a convergence criterion of 10^{-4} for each scaled residual component. The phase-coupled SIMPLE (PC-SIMPLE) algorithm [23], which is an extension of the SIMPLE algorithm to multiphase flows, was applied for the pressure-velocity coupling.

In this algorithm, the coupling terms were treated implicitly and form part of the solution matrix. The pressure-velocity coupling was based on total volume continuity and the effects of the interfacial coupling terms were fully incorporated into the pressure correction equation. The Gauss-Seidel method was applied to solve these equations, which can be stable due to point by point iteration. In order to reduce the number of iterations and to accelerate the convergence of solution, an algebraic multigrid (AMG) scheme was also used to coarsen the grids [24].

3.2 Boundary and Initial Conditions

The main conditions that are applied to the simulation of the fuel reactor are listed in Tabs. 1 and 2. The k–ε turbulence models were selected. The drag coefficient between the gas phase and solid phase that was used was proposed by Wen and Yu [19]. The restitution coefficient between the solid particles was 0.9. The heat transfer coefficient between the gas phase and solid phase that was used was proposed by Gunn [17]. The velocity-inlet condition for the inlet of reactor and outflow condition for the outlet of reactor were chosen as the boundary conditions. A zero gradient condition was used for the turbulent kinetic energy at the walls. The no-slip wall condition was used for both the gas and solid phases [16]. The simulations were carried out with the finite volume method (FVM), in which the inter-phase slip algorithm (IPSA) of

Table 1. Simulation model parameters (fuel reactor).

Description	Value	Comment
Particle Density (kg/m^3)	2960	Calcium sulfate
Gas Density(kg/m^3)	0.08189/1.225	Hydrogen/Nitrogen
Initial Solids Packing	0.48	Fixed value
Bed Width (m)	0.25	Fixed value
Bed Height (m)	1	Fixed value
Static Bed Height (m)	0.4	Fixed value
Inlet Boundary Conditions	Velocity	Superficial gas velocity
Outlet Boundary Conditions	Outflow	Fully developed flow
Time Steps (s)	0.0001	Specified
Convergence Criteria	10^{-4}	Specified
Maximum Number of Iterations	10	Specified

Spalding and Markatos [25] was used to solve the velocity-pressure coupled differential equations. The second-order QUICK scheme was used for the evaluation of the convective terms. The time step was set as 0.0001 s.

As shown in Fig. 3, the bed was initially filled with particles to a height of 0.4 m, where the total volume fraction of solids was patched as 0.48 [26]. The maximum particle packing was chosen as $\varepsilon_{s,max} = 0.6$ to prevent the spacing between particles from decreasing to zero [27]. In addition, the 2D computational domain was discretized by 10,000 rectangular cells. The grid size ($D_x \cdot D_y$) was 0.5 cm · 0.5 cm.

4 Computational Results and Discussion

Twelve different cases were designed to study the effects of three parameters including temperature, particle diameter and the flow rate. Cases 1–4 were used to study the effect of the particle diameter on CLC performance, cases 5–8 were used to study the effect of the flow rate on CLC performance, and cases 9–12 were used to study the effect of the temperature on CLC performance. In order to investigate the effect of one parameter, all other parameters should be kept constant. Therefore, to study the effect of particle diameter, i.e., 0.2 mm or 0.3 mm, temperature and the flow rate were kept constant at values of 1173 K and 52.3 Nm^3/h, respectively. In order to study the effect of flow rate range between 39.7–83.7 Nm^3/h, temperature and particle diameter were kept constant at 1173 K and 0.275 mm, respectively. Finally, in order to study the effect of the temperature range from 1123–1248 K, the particle diameter and the flow rate were kept constant at values of 0.275 mm and 52.3 Nm^3/h, respectively. Tab. 2 lists the range of operating conditions that were applied to these cases.

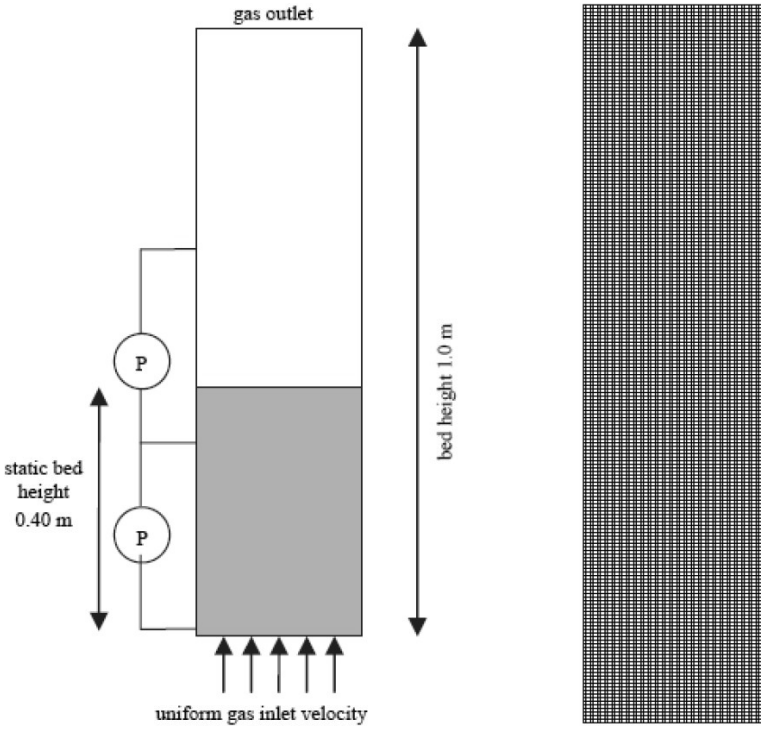

Figure 3. Schematic diagram of the experimental setup.

4.1 Distributions of Solid Volume Fraction and Gas Composition in the Fuel Reactor

Fig. 4 shows the distributions of the solid volume fraction and gas composition for the eight cases involved. As shown in Fig. 4. A feed fuel gas consisting of H_2 and N_2 is fed into the reactor through a distributor. The upward flowing gas bubbles provide the energy to keep the oxygen carrier and fuel gas highly mixed. The bubble formation is well captured by CFD simulation. Most of the salient bubble features, e.g., formation, rise and burst, can be observed from the simulated frame in Fig. 4, where blue represents pure gas and red mimics a dense gas-solid mixture. These features influence the amount of fuel burned since fast bubbles lead to a lower reactant conversion rate. The computed flow patterns due to the bubble predict a global mixing between the gas phase and solid phase in the fuel reactor. Fig. 4 also shows the distributions of reactant and product in terms of molar fraction in the gas phase in the quasi-steady state condition at 6 s. The reactant, H_2, from the gas phase reacts with oxygen, O_2, from the oxygen carrier and is converted to the gaseous water product, H_2O. The concentration of H_2 decreases along the height of the reactor, while the concentration of H_2O increases and reaches a maximum in the dense bed region. In the free board area, the changes of molar fraction of the gas compositions are not as obvious as in the dense bed. A possible reason for this is that the reaction rates slow down due to the lower solids concentration.

In order to obtain a better understanding of the system, case 3 is chosen for careful examination. From Fig. 4, it can be seen that the profile of the reactant, H_2, decreases linearly from ca. 0.25 around the distributor to 0.042 as a function of bed height. Fig. 4 also shows a relation between bubble formation and fuel gas reaction, described by the solid volume fraction and the molar fraction of products in the gas phase, respectively. It can be

Table 2. Range of operating conditions for the simulations.

Bed Temperature (°C)	Molar Fraction of H_2 (Inlet)	Gas Flow Rate (Nm^3/h)	Particle Diameter (mm)
850-975	25 %	39.7–83.7	0.2–0.3

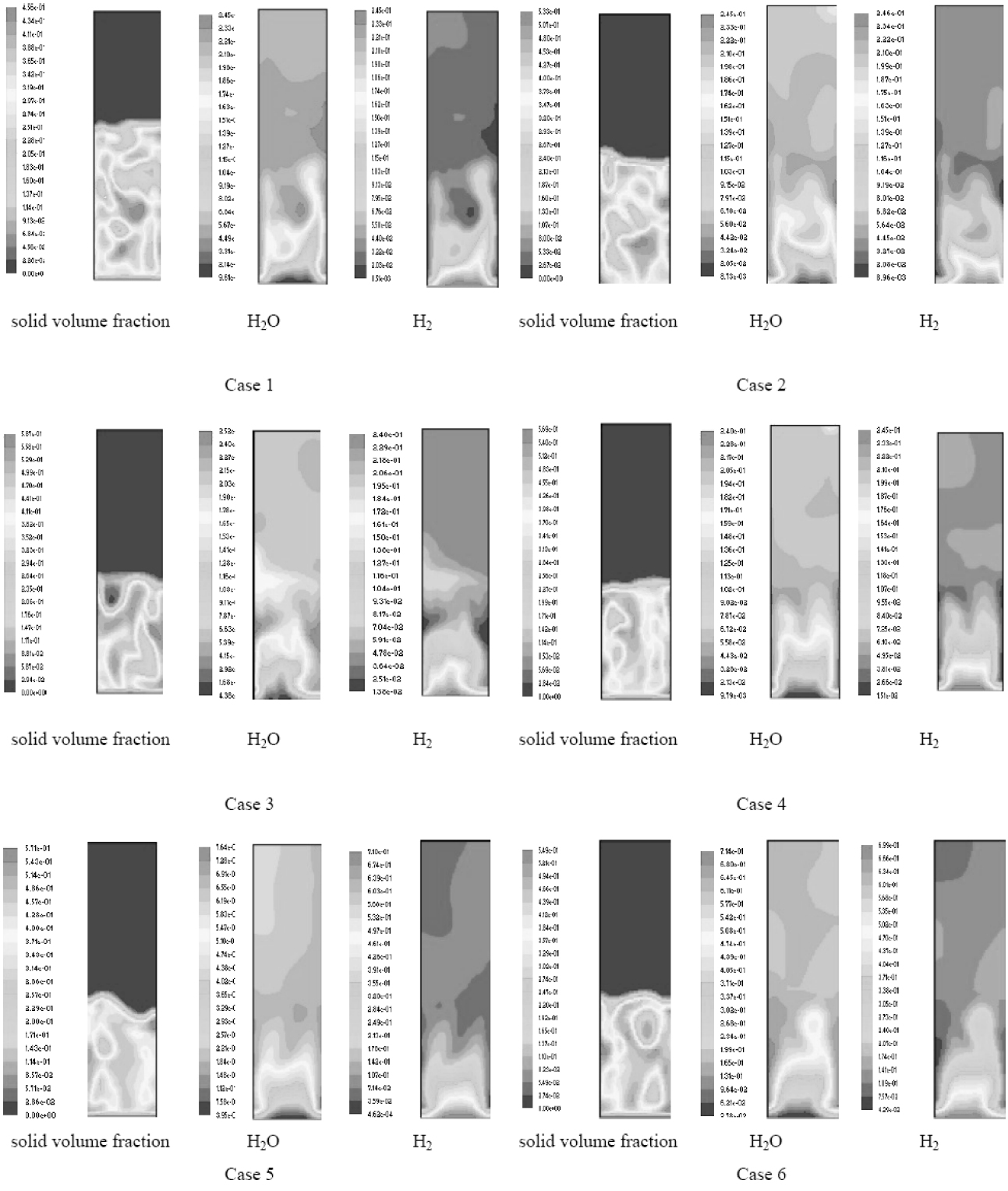

Figure 4. The distributions of the solid volume fraction and gas composition.

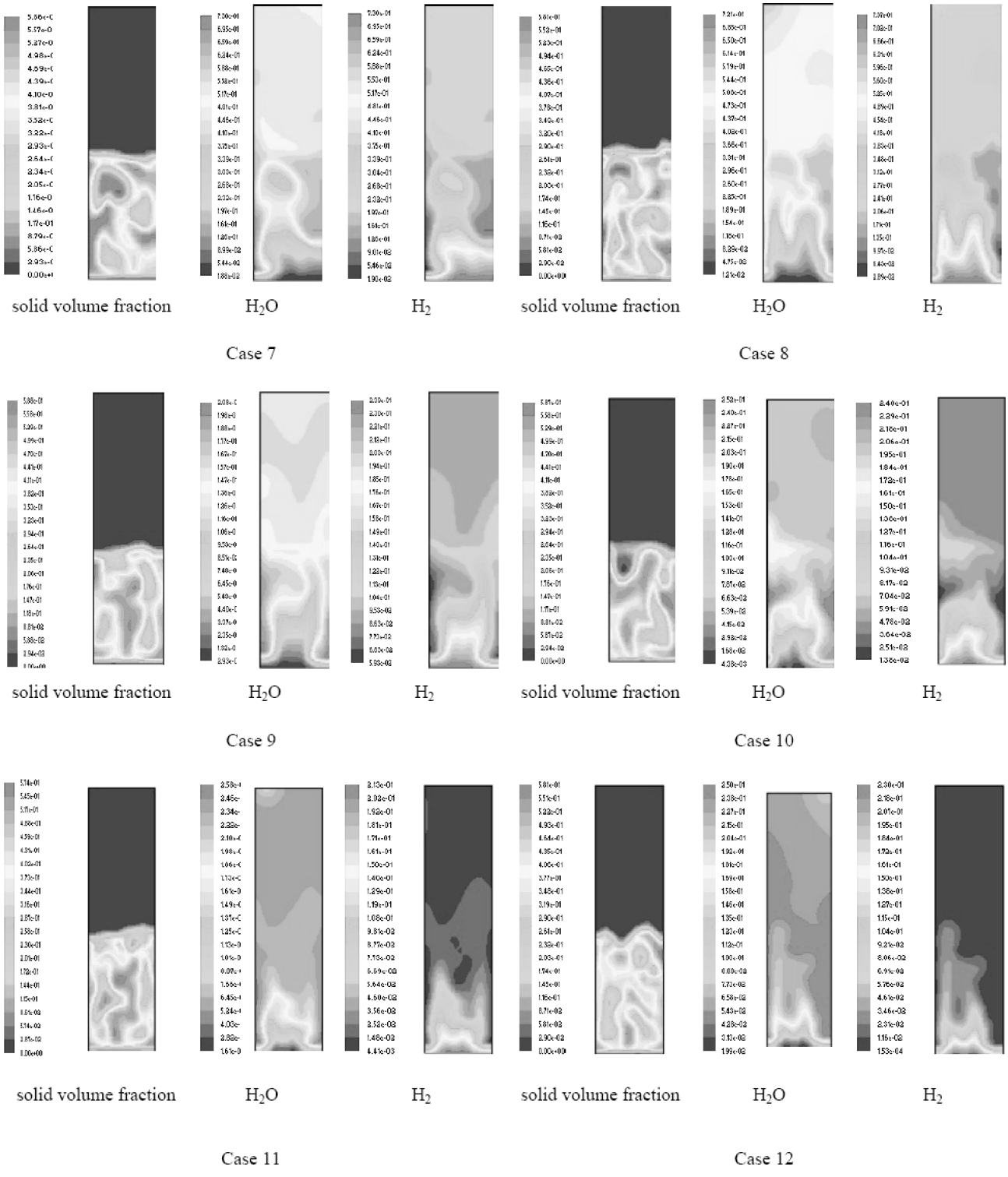

Figure 4. Continued.

seen that products produced by the reduction-reaction are higher at the immersion phase where the solid volume fraction is high, while reactant H_2 levels are higher at the bubble phase. The reaction in the fuel reactor depends significantly on the concentration of the oxygen carrier.

Fig. 5 shows the oscillations of fuel gas reactant in the dense bed region at $x = 0$ cm and $y = 25$ cm. The intense oscillations are due to bubble passage and reaction in the dense region. The hydrogen molar fraction sustains an oscillation of ca. 0.07. Fig. 6 shows similar oscillations for the gas product, i.e., water vapor. As expected, the product concentration rapidly increases when the reactant is injected at 0.5 s. However, at ca. 2 s, the products concentration no longer increases and the water vapor molar fraction oscillates at ca. 0.2. This trend indicates that the reaction reaches quasi-equilibrium after 2 s.

The molar fractions of reactant and products in the outlet of the bed are shown in Fig. 7. As expected, the products concentration increases rapidly when the reactant is injected at 2.5 s. The gas molar fraction becomes almost constant at ca. 0.042 for H_2 and 0.21 for H_2O. This is due to the absence of solid reactant $CaSO_4$ in the free board region and to the absence of bubbles. The conversion of H_2 is ca. 83.2 %, under these simulation conditions.

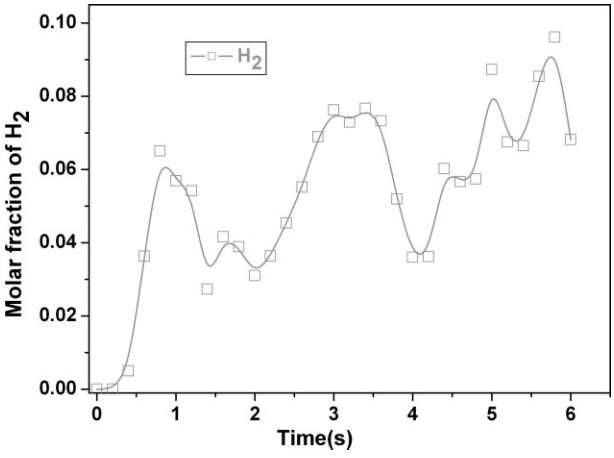

Figure 5. Molar fraction of H_2 at a point in the fluidized-bed regime, 0 cm (*x*) and 25 cm (*y*).

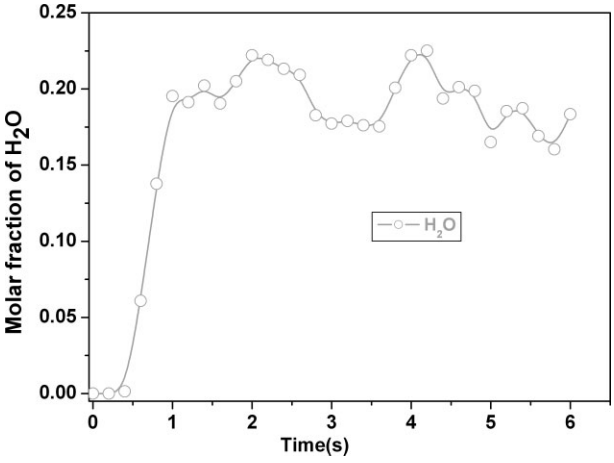

Figure 6. Molar fraction of H_2O at a point in the fluidized-bed regime, 0 cm (*x*) and 25 cm (*y*).

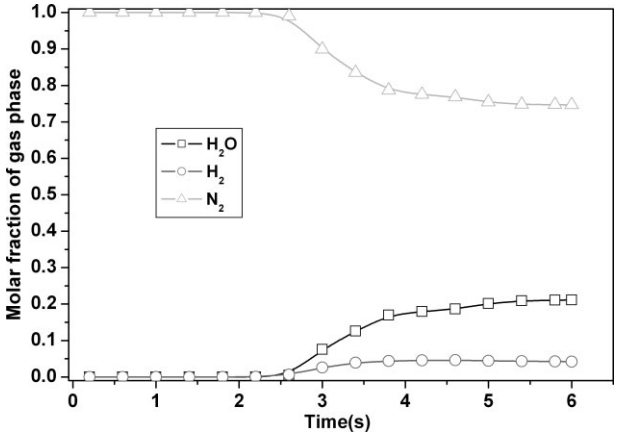

Figure 7. Molar fractions of the outlet gas phase.

4.2 Effect of Particle Diameter

Cases 1–4 are designed to study the effect of the particle diameter on CLC performance. The particle size is changed from 0.2 mm to 0.3 mm to study the influence on reduction reactivity. The effect of particle diameter on the molar fractions of H_2 and H_2O in the gas phase as a function of time are shown in Figs. 8 and 9. Clearly, the particle size has an influence on the reduction reaction. The molar fraction of H_2 is 4.72 % for 0.3 mm particle diameter and decreases to 2.82 % for a diameter of 0.2 mm. The content of H_2O is ca. 19.67 % at 0.3 mm and increases to 22.8 % for 0.2 mm, respectively. These results illustrate that a certain decrease of particle size increases the reduction reactivity. Fig. 10 shows the effect of particle size on the gas conversion. The decrease in the particle size resulted in

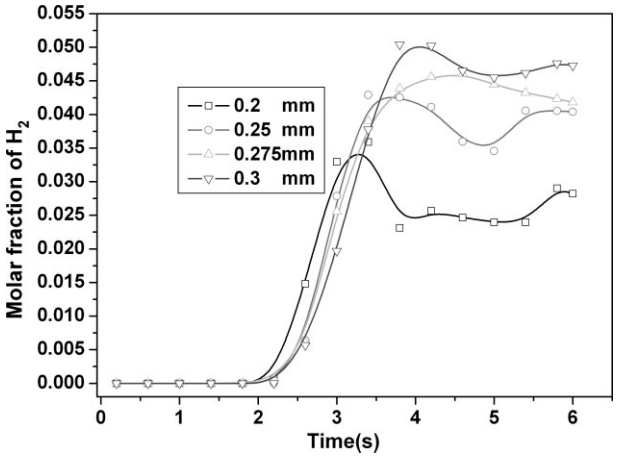

Figure 8. Effect of particle diameter on the molar fraction of outlet H_2.

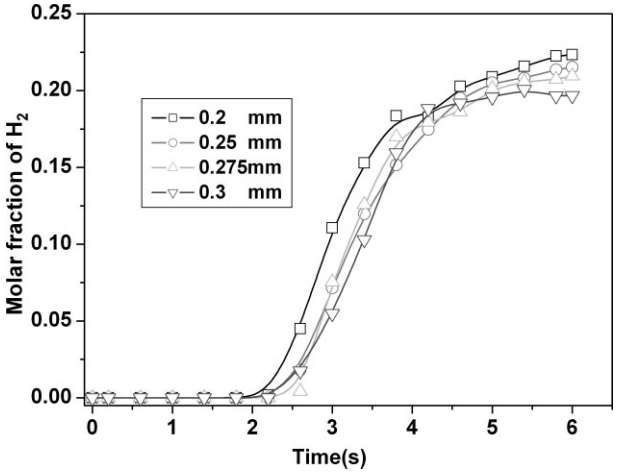

Figure 9. Effect of particle diameter on the molar fraction of outlet H_2O.

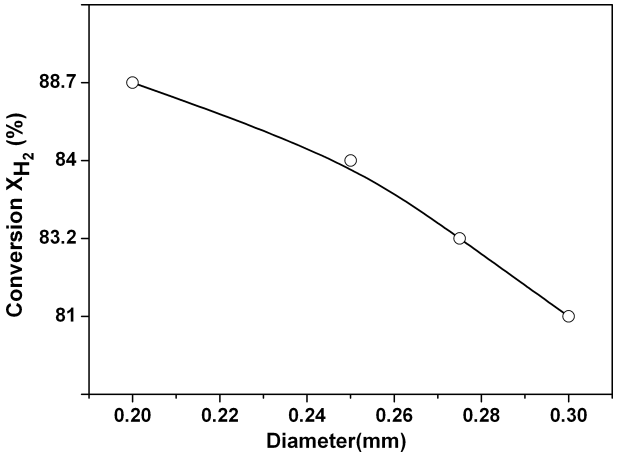

Figure 10. Effect of particle diameter on the conversion of H_2.

an increase in the conversion of H_2. The conversion of H_2 is 81 % for 0.3 mm and increases to 88.7 % for 0.2 mm. The results show that small particles have a greater surface area for the contact between the gases and solid, which will result in increased conversion of H_2.

4.3 Effect of Flow Rate

To investigate the effect of gas flow rate on the reduction reaction, cases 5–8 are performed with different fuel gas flow rates ranging between 39.7–83.7 Nm^3/h. The calculation results of the outlet gas composition as a function of fuel flow rate are shown in Figs. 11 and 12. Figs. 11 and 12 show that the molar fraction of H_2O decreases significantly from 62.8 % to 47.9 % and the H_2 molar fraction increases from 6.7 % to 26.9 % as the gas flow rate increases between 39.7–83.7 Nm^3/h. A possible reason is that the residence time increases at a smaller gas flow rate and results in an increase in the gas/solid reaction

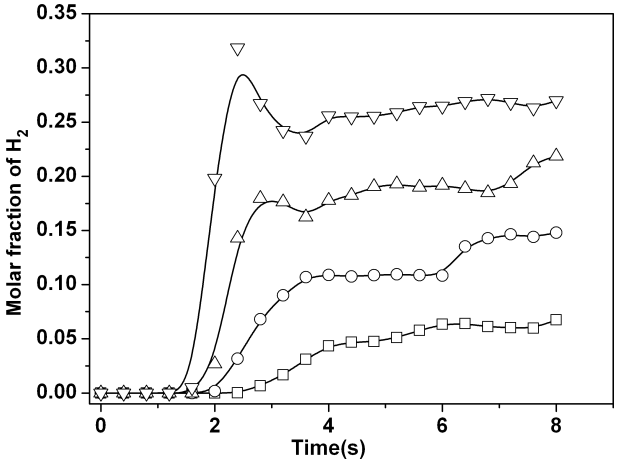

Figure 11. Effect of flow rate on the molar fraction of outlet H_2 (39.7 Nm^3/h (-□-), 52.3 Nm^3/h (-○-), 66.9 Nm^3/h (-△-), and 83.7 Nm^3/h (-▽-)).

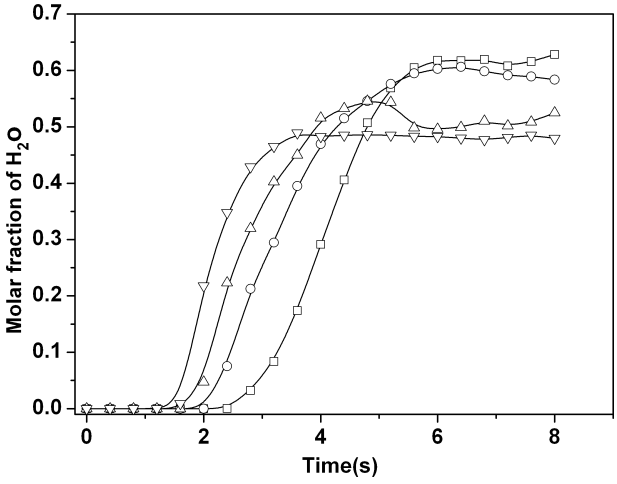

Figure 12. Effect of flow rate on the molar fraction of outlet H_2O (39.7 Nm^3/h (-□-), 52.3 Nm^3/h (-○-), 66.9 Nm^3/h (-△-), and 83.7 Nm^3/h (-▽-)).

time. Fig. 13 displays the effect of the flow rate on the conversion of H_2. The increase in the flow rate results in an decrease of the conversion of H_2. The conversion of H_2 is 91 % for 39.7 Nm^3/h and decreases to 64 % for 83.7 Nm^3/h. The results show that a smaller gas flow rate results in a longer residence time in the bed and leads to an increase in gas/solid reaction time, which increases the conversion of H_2.

4.4 Effect of Bed Temperature

Bed temperature is one of the most important operating parameters affecting the performance of CLC, since the reaction rate is greatly accelerated by increasing temperature. Cases 9–12 are designed to study the effect of temperature on CLC performance. The bed temperatures chosen are 850, 900, 950 and

975 °C, respectively. The calculation results for the outlet gas compositions are shown in Figs. 14 and 15. These figures also demonstrate the effect of the bed temperature on the molar fraction of H_2 and H_2O at the outlet. The outlet molar fraction of hydrogen decreases from 0.0944 to 0.0098 as the bed temperature increases from 850 °C to 975 °C. On the contrary, the outlet molar fraction of H_2O increases slightly from 0.154 to 0.246. One possible reason for this change is that the increase of bed temperature will increase the rate of reaction (1). This means that much more H_2 will be consumed by $CaSO_4$ and more and more H_2O will be produced. Fig. 16 displays the effect of bed temperature on the conversion of H_2. It is observed that the conversion of H_2 increases at higher temperatures. The conversion of hydrogen at the values of 850, 900, 950 and 975 °C are 62.24, 83.27, 94.6 and 96.6 %, respectively. It can be concluded that the bed temperature is the most important operating parameter for the reduction reaction.

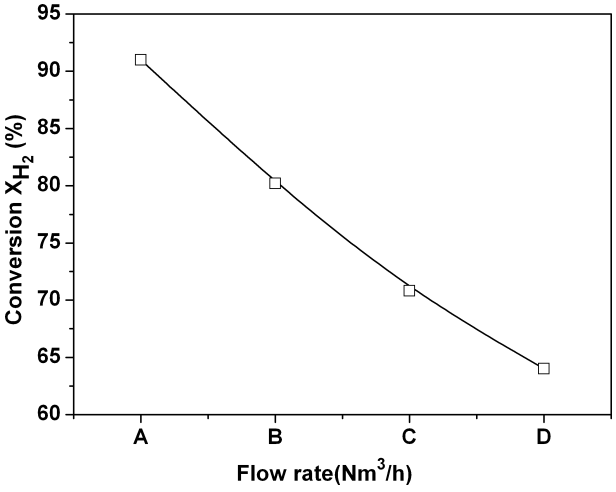

Figure 13. Effect of flow rate on the conversion of H_2 (A (39.7 Nm^3/h), B (52.3 Nm^3/h), C (66.9 Nm^3/h), D (83.7 Nm^3/h)).

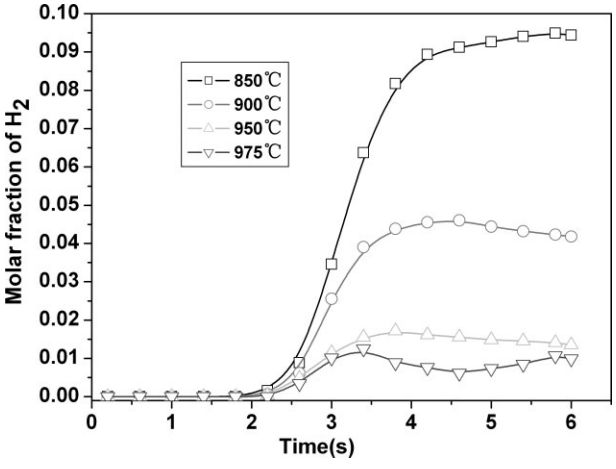

Figure 14. Effect of temperature on the molar fraction of outlet H_2.

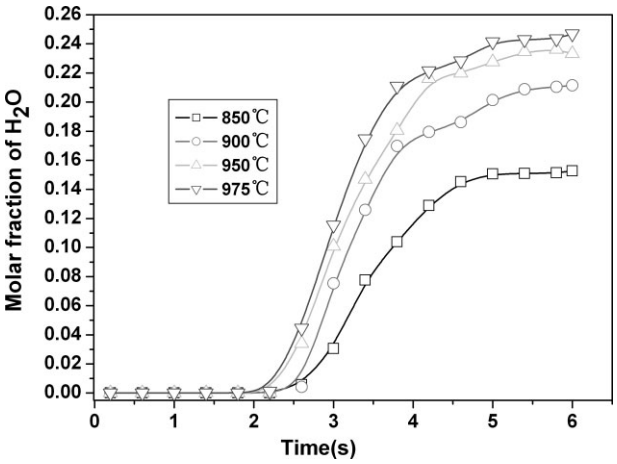

Figure 15. Effect of temperature on molar fraction of outlet H_2O.

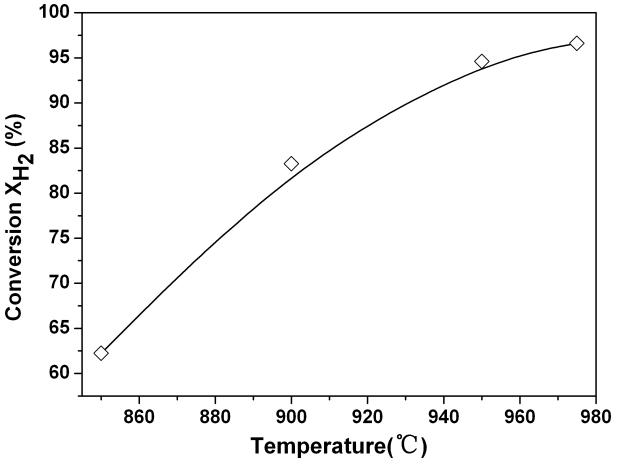

Figure 16. Effect of bed temperature on the conversion of H_2.

5 Conclusions

A model was presented that described multiphase hydrodynamics based on the kinetic theory of granular temperature applied to a fuel reactor for a CLC process. A recent thorough literature review demonstrates that multiphase fluid dynamics modeling for CLC by FLUENT code is not available in the open literature.

2D CFD modeling of fuel reactor was developed. The distributions of the solid volume fraction and gas composition in the reactor were presented. The effects of the particle size and temperature on CLC performance were also predicted.

The concentration of H_2 decreased along the height of the reactor, while the concentration of H_2O increased and reached a maximum in the dense bed region. In the free board region, the changes of molar fraction of the gas compositions were not as obvious as in the dense bed. The effect of particle diameter was obvious on CLC performance. The conversion of H_2 was 81 % for 0.3 mm diameter and increased to 88.7 % for 0.2 mm diameter. Lower gas flow rates increased the conversion of H_2,

since the residence time increased and resulted in an increase in the gas/solid reaction time. The effect of the bed temperature was also obvious on CLC performance. The conversion of H_2 increased greatly from 62.4 % at 850 °C to 96.6 % at 975 °C. Bed temperature was shown to be the most important operating parameter affecting the performance of CLC.

The critical component of the system, i.e., the fuel reactor, was also modeled in a similar manner to circulating fluidized-bed combustor simulations where the riser was initially modeled prior to the complete loop. However, it is valuable to couple the fuel reactor with other components, e.g., the air reactor and cyclone, to model the complete loop system since the heat integration between chemical looping reactors is a very important feature in the development of this novel technology, which can exploit the existing circulating fluidized-bed technology.

Acknowledgments

This work was financially supported by the National Natural Science Foundation of China (Grant No. 50606006) and the Hi-tech Research and Development Program of China (863 Program, 2006AA020101).

Symbols used

d_p	[m]	diameter
$D_{m,i}$	[m^2/s]	diffusion coefficient of the mixture
e	[–]	coefficient of restitution
E	[kJ/kmol]	activation energy
g_0	[–]	radial distribution function
g	[m/s^2]	gravity
h_{sg}	[W/m^2 K]	heat transfer coefficient
H_i	[J/kg]	enthalpy
I_{2D}	[–]	second invariant of the deviatoric stress tensor
$J_{g,i}$	[kg/m^2 s]	diffusion flux
$k_{\Theta s}$	[kg/s m]	diffusion coefficient for granular energy
K_i	[1/kPa s]	apparent kinetic constant
k_g	[W/m K]	thermal conductivity of gas
Nu	[–]	Nusselt number
Pr	[–]	Prandtl number
P	[Pa]	Pressure
P_s	[Pa]	solid phase pressure
Q_{sg}	[W/m^2]	intensity of heat exchange between the gas phase and solid phase
Re	[–]	Reynolds number
$R_{s,i}$	[kmol/m^3 s]	heterogeneous reaction rate
$R_{g,i}$	[kmol/m^3 s]	homogeneous reaction rate
r_c	[kmol/m^3 s]	reaction rate
Sc	[–]	Schmidt number
S	[–]	source term
T	[K]	temperature
t	[s]	time
u	[m/s]	mean velocity
u'_s	[m/s]	fluctuating velocity of particles
V	[m/s]	instantaneous velocity
X_i	[–]	molar fraction
Y_i	[–]	mass fraction
Z_i	[–]	conversion

Greek symbols

ε	[–]	volume fraction
ρ	[kg/m^3]	density
λ	[W/m K]	thermal conductivity of mixture
τ_g	[Pa]	stress tensor
τ_i	[s]	time
η	[kg/s m]	dynamic viscosity
γ	[W/m^3]	dissipation of fluctuation energy
Θ_s	[m^2/s^2]	granular temperature
β	[kg/m^{3}s]	the drag coefficient
μ_s	[kg/m s]	solid shear viscosity
$\mu_{s,col}$	[kg/m s]	solid collision viscosity
$\mu_{s,kin}$	[kg/m s]	kinetic viscosity
$\mu_{s,fr}$	[kg/m s]	solid frictional viscosity
ξ_s	[Pa s]	solid bulk viscosity
ϕ	[kg/s^3 m]	transfer rate of kinetic energy
$\rho_{m,CaSO_4}$	[mol/m^3]	molar density of $CaSO_4$

Subscripts

s	solid phase
g	gas phase
i	the i^{th} species
I, j, k	direction coordinate

References

[1] H. J. Richter, K. F. Knoche, in *ACS Symp. Ser. 235*, Washington DC **1983**.
[2] M. Johansson, T. Mattisson, M. Rydén, A. Lyngfelt, *Int. Seminar on Carbon Sequestion and Climate Change*, Rio de Janeiro, Brazil, October **2006**.
[3] H.-J. Ryu et al., *Korean J. Chem. Eng.* **2001**, *18*, 831.
[4] M. Ishida, M. Yamamoto, T. Ohba, *Energy Convers. Manage.* **2002**, *43*, 1469.
[5] J. Adánez et al., *17th Int. Fluidized-bed Combustion Conf.*, Jacksonville, FL, May **2003**.
[6] J. Adánez et al., *Energy Fuels* **2004**, *18 (2)*, 371.
[7] T. Mattisson, M. Johansson, A. Lyngfelt, *Energy Fuels* **2004**, *18*, 628.
[8] P. Cho, T. Mattisson, A. Lyngfelt, *Fuel* **2004**, *83*, 1215.
[9] A. Abad, T. Mattisson, A. Lyngfelt, M. Rydén, *Fuel* **2006**, *85*, 1174.
[10] E. Johansson, T. Mattisson, A. Lyngfelt, H. Thunman, *Fuel* **2006**, *85*, 1428.
[11] T. Mattisson, A. Jardnas, A. Lyngfelt, *Energy Fuels* **2003**, *17*, 643.
[12] L.-H. Shen, M. Zheng, *Combust. Flame* **2008**, *154*, 489.
[13] S. Cooper, C. J. Coronella, *Powder Technol.* **2005**, *151*, 27.
[14] S. Ravelli, A. Perdichizzi, G. Barigozzi, *Prog. Energy Combust. Sci.* **2008**, *34*, 224.
[15] A. Frazeli, M. Behnam, *AIChE J.* **2007**, *5*, A93.
[16] J. Ding, D. Gidaspow, *AIChE J.* **1990**, *32 (1)*, 523.

[17] D. J. Gunn, *Int. J. Heat Mass Transfer* **1978**, *21*, 467.
[18] D. J. Patil, M. S. Annaland, J. A. M. Kuipers, *Chem. Eng. Sci.* **2005**, *60*, 57.
[19] C.-Y. Wen, Y.-H. Yu, *Chem. Eng. Prog. Symp.* **1966**, *62*, 100.
[20] B.-S. Kim, H. Y. Sohn, *Eng. Chem. Res.* **2002**, *41*, 3092.
[21] Q. Zafar, A. Abad, T. Mattisson, B. Gevert, *Chem. Eng. Sci.* **2007**, *62*, 6556.
[22] J. E. Readman, A. Olafsen, J. B. Smith, R. Blom, *Energy Fuels* **2006**, *20*, 1382.
[23] S. A. Vasquez, V. A. Ivanov, *ASME 2000 Fluids Engineering Division Summer Meeting*, Boston, MA **2000.**
[24] W. Q. Tao, *Recent Advance of Numerical Heat Transfer*, Science Press, Beijing **2000**.
[25] D. B. Spalding, N. C. Markatos, *Int. J. Physiochem. Hydrodynam.* **1983**, *323*, 4.
[26] F. Chejne, J. P. Hernandez, *Fuel* **2002**, *81*, 1687.
[27] H. Enwald, A. E. Almstedt, *Chem. Eng. Sci.* **1999**, *54*, 329.

